

Supporting Information for "Importance of considering near-surface attenuation in earthquake source parameter estimation: Insights from Kappa at a dense array in Oklahoma"

Hilary Chang, Rachel E. Abercrombie, and Nori Nakata

December 10, 2024

Contents

1. Text S1 and S2
2. Figures S1 to S10
3. Tables S1 to S2

Text S1 Calculating the Fourier acceleration spectra

Before cutting the arrivals, we cut the raw data approximately 1 minute before to 2 minutes after the first arrival time. Then, we preprocess the 3-minute trace:

1. Demean and detrend.
2. Taper both ends of the time series (5% each side).
3. Prefilter between 0.006 and 150 Hz (taper out to 0.005 and 250 Hz).
4. Remove instrument response and convert to acceleration using Obspy (Beyreuther et al., 2010) and the response file provided by the manufacturer (with a water level of 40 to suppress noises below 1 Hz).

We use the Taup raytracing module in Obspy to estimate arrival times using the velocity model from Rubinstein et al. (2018). After visually checking the moveouts, we find small time shifts between the predicted and actual arrivals (< 0.3s for P arrivals and < 1.5s for S arrivals). We manually adjust the arrival times for each event based on the observed arrivals. We stack all the spectra in a subarray (15 – 20 stations).

Text S2 Spectral fitting for local earthquakes

Here are the processing steps for refit tests 1 – 3 for local earthquakes. The preprocessing before calculating the Fourier acceleration spectra are:

1. Demean and detrend.
2. Taper both ends of the time series (5% each side).
3. Prefilter between 0.006 and 150 Hz (taper out to 0.005 and 250 Hz).
4. Remove instrument response and convert to displacement using Obspy (Beyreuther et al., 2010) and the response file provided by the manufacturer (with a water level of 60 to suppress noises below 1 Hz).

We cut the P wave spectra in a 0.8 s time window (-0.2 to 0.6 s around the P arrival). The arrival times are based on the catalog from Cochran et al. (2020). We discard any clipped traces and remove data points with a signal-to-noise ratio (SNR) of less than 9. We discard spectra that do not have a continuous portion left after the point-wise data removal. We resample the remaining spectra to a constant interval along the log-frequency scale. We group the stations into 272 subarrays. Each subarray consists of stations within a 2.5 km diameter circle. We stack the resampled spectra among stations within each subarray. We use LmFIT (Newville et al., 2016) to do the single-spectra fitting on the stacked spectra for each subarray.

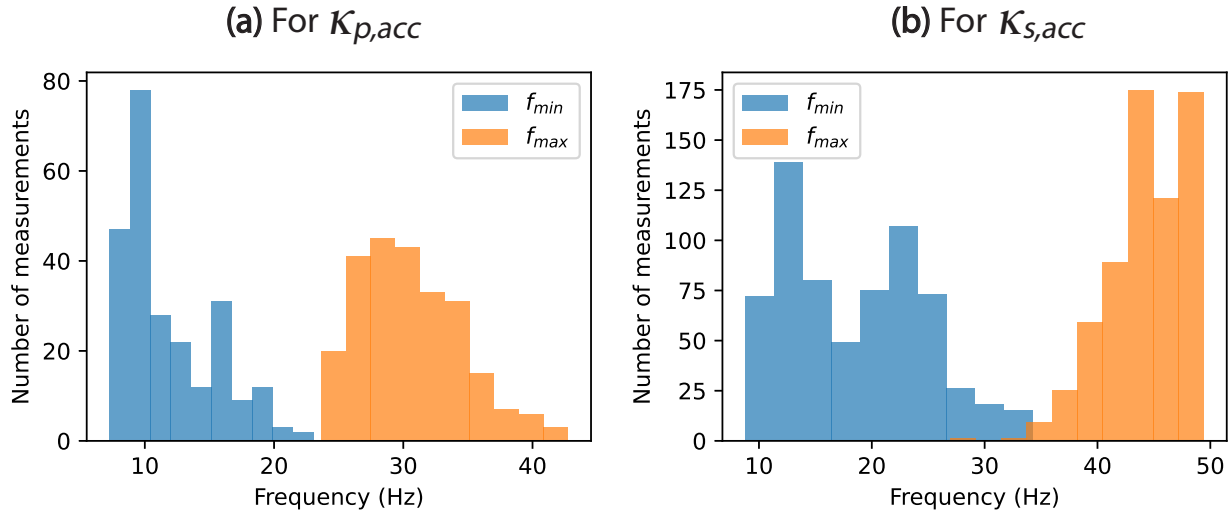


Figure S1. The frequency ranges for estimating (a) $\kappa_{p,acc}$ and (b) $\kappa_{s,acc}$. The minimum frequency (f_{min}) is defined by the lowest first derivative on the degree-15 polynomial that fits the acceleration spectra (Nye et al., 2023), or 5 Hz (above the corner frequency), depending on which is higher. The maximum frequency (f_{max}) is where the signal-to-noise ratio drops below 3 (Ktenidou et al., 2016). Finally, we only retain measurements with $f_{max} - f_{min} > 15$ Hz. The histograms include measurements of events R1 – R3 that meet these criteria.

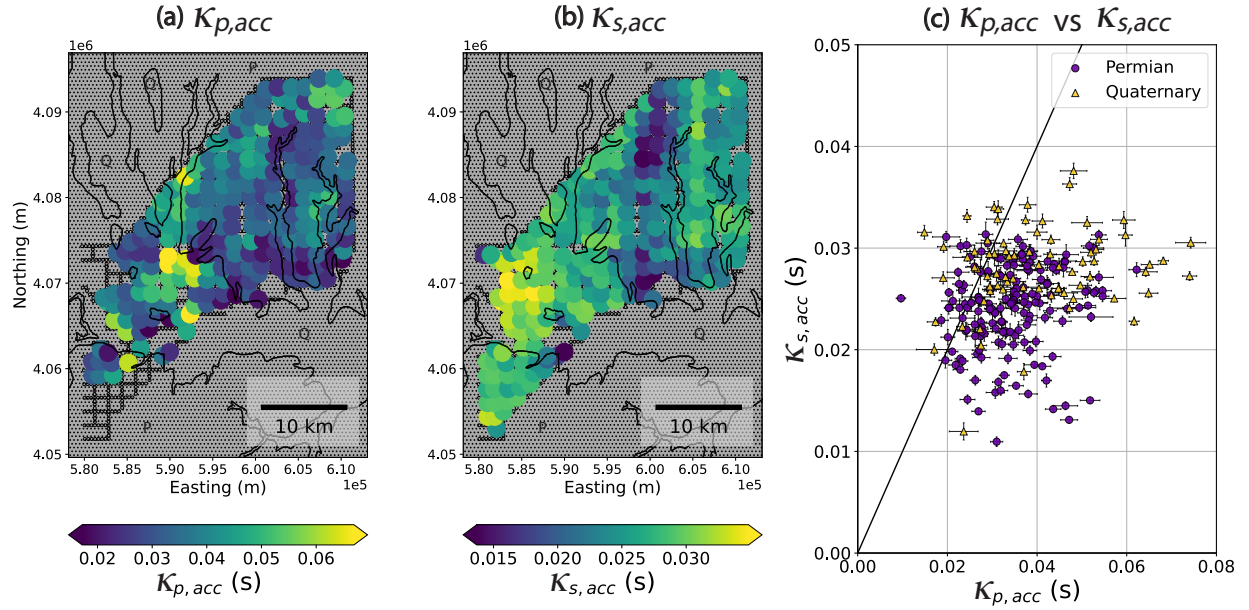


Figure S2. High-frequency spectral decay parameter kappa (vertical component): (a) $\kappa_{p,acc}$ and (b) $\kappa_{s,acc}$, and (c) $\kappa_{p,acc}$ vs $\kappa_{s,acc}$. This figure is similar to Figure 4 but here, we relax the minimum frequency range to 10 Hz to include more measurements on the Quaternary sites. The largest $\kappa_{p,acc}$ and $\kappa_{s,acc}$ are on the Quaternary sites (orange dots in (c)). The values are the median of events R1 and R2. In (a) and (b), each colored circle represents a subarray consisting of stations within a 2.5 km diameter circle (15 – 20 stations; small black hollow circles). The color ranges exclude the 1% lowest and highest values for visualization. The contours indicate the boundaries of the surficial Quaternary formations (Q) versus the Permian formations (P).

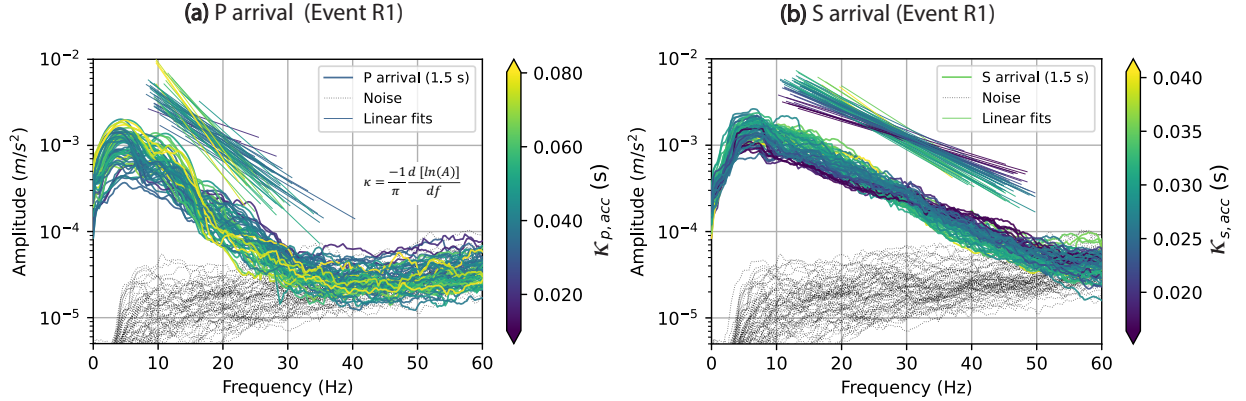


Figure S3. High-frequency spectral decay parameter kappa (κ) measured from the vertical component of the acceleration spectra of regional event R1. (a) P-arrival for $\kappa_{p,acc}$, and (b) S-arrival for $\kappa_{s,acc}$. This figure is similar to Figure 3 but here, we relax the minimum frequency range to 10 Hz to include more measurements on the Quaternary sites. The $\kappa_{p,acc}$ measurements might be subject to amplitude bulges between 10 and 20 Hz. The spectra are stacked among stations within a subarray of a 2.5 km diameter circle (15 – 20 stations). The signal spectra (colored) are calculated in a 1.5 s window around the P- or S-arrivals. The noise spectra (dotted black) are calculated in a 1.5 s window that is 8 s before the P arrivals. The thin colored lines are linear fits for estimating kappa. Only one-fourth of the total spectra and fitting are shown (equally spaced across the array) for visualization.

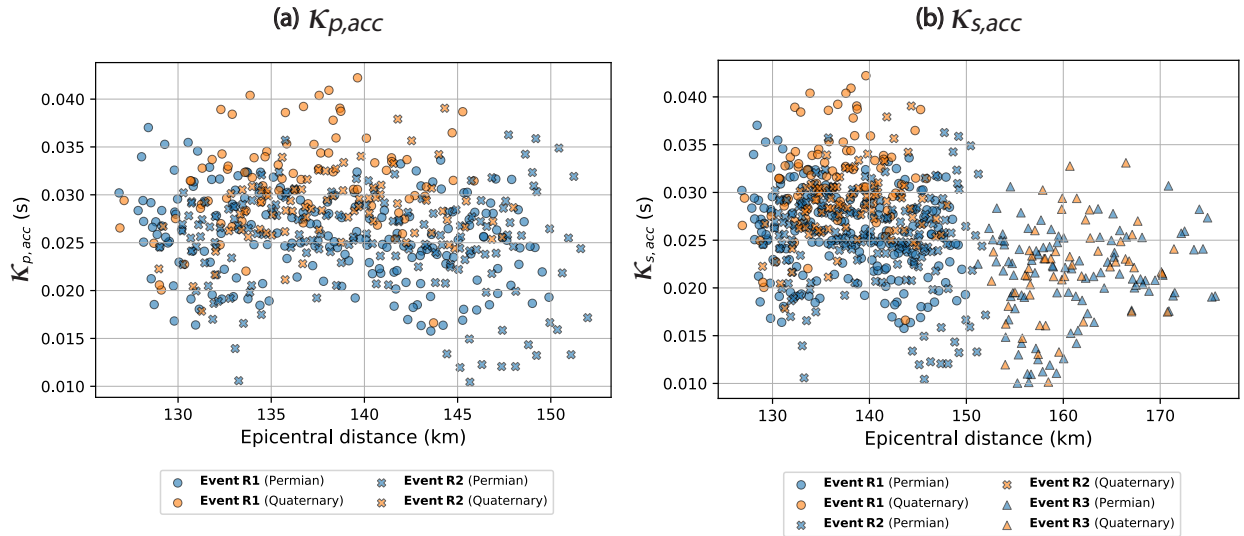


Figure S4. Distance versus the high-frequency spectral attenuation parameter (a) $\kappa_{p,acc}$ and (b) $\kappa_{s,acc}$ (vertical component). Each point is a measurement from the stacked acceleration spectra among stations in a subarray for an event (R1, R2, R3). The subarrays consist of stations within a circle of 2.5 km diameter (15 – 20 stations). Blue and yellow indicate the dominant surficial formation (Permian or Quaternary) under the subarray. We do not observe a clear positive distance dependence for $\kappa_{p,acc}$ and $\kappa_{s,acc}$ because of the small data distance range and the large variability of measurements. The Quaternary sites generally have higher attenuation.

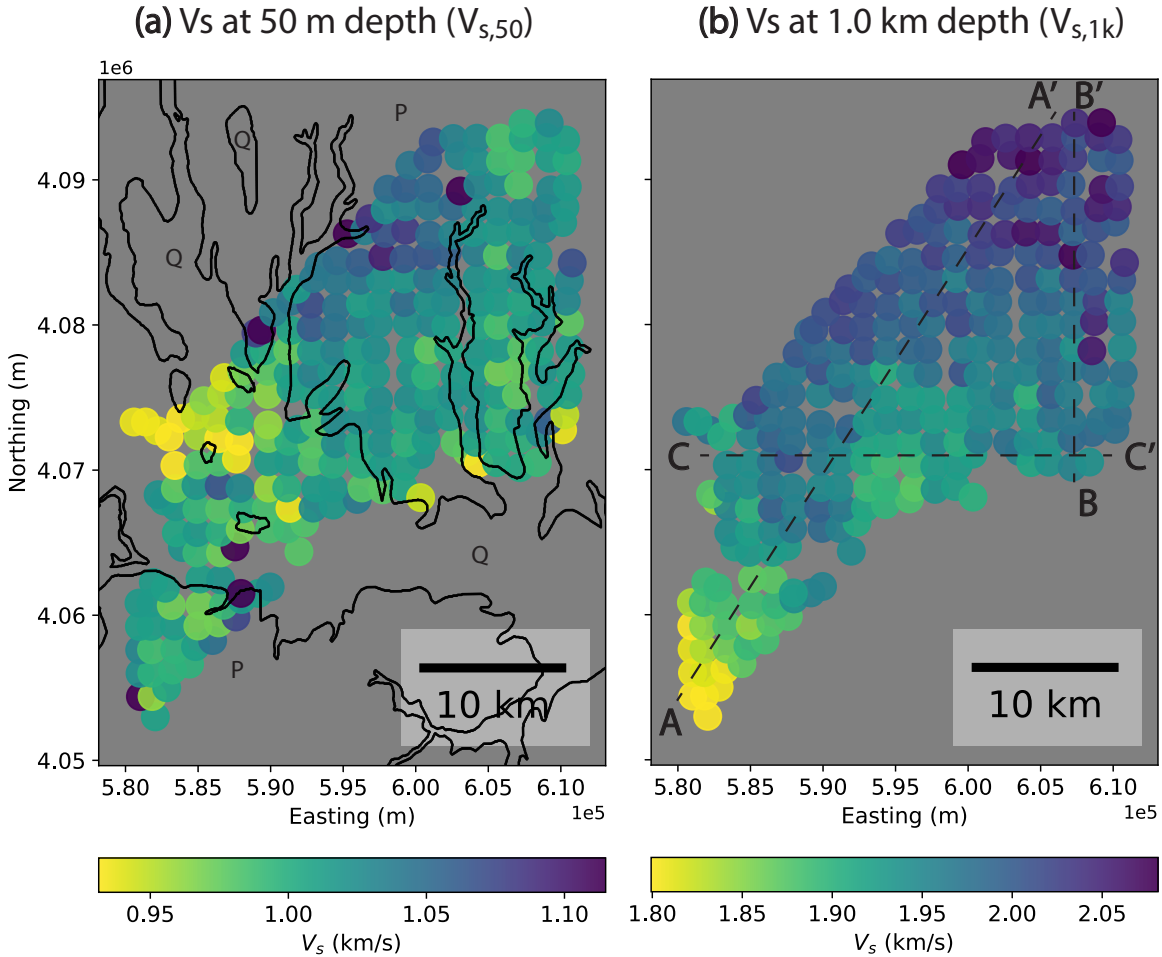


Figure S5. Shear-wave velocity (V_s) from the ambient noise surface wave analysis in Chang et al. (2024). **(a)** V_s at 50 m ($V_{s,50}$), and **(b)** V_s at 1.0 km ($V_{s,1k}$). Each colored circle represents a station group. The color bars omit the 2% lowest and highest values for visualization. The contours indicate the boundaries of the surficial Quaternary formations (Q) versus the Permian formations (P). See Figure S6 for cross-sections along A–A', B–B', and C–C'. The V_s shows gentle lateral transitions with slightly different patterns at 50 m and 1.0 km depths. Due to bandwidth limits, we do not have good resolution in the upper 50 m. However, the Quaternary formations which are in the upper 5–30 m based on Johnson & Luza (2008) likely produce local low velocity zones within the very shallow depths.

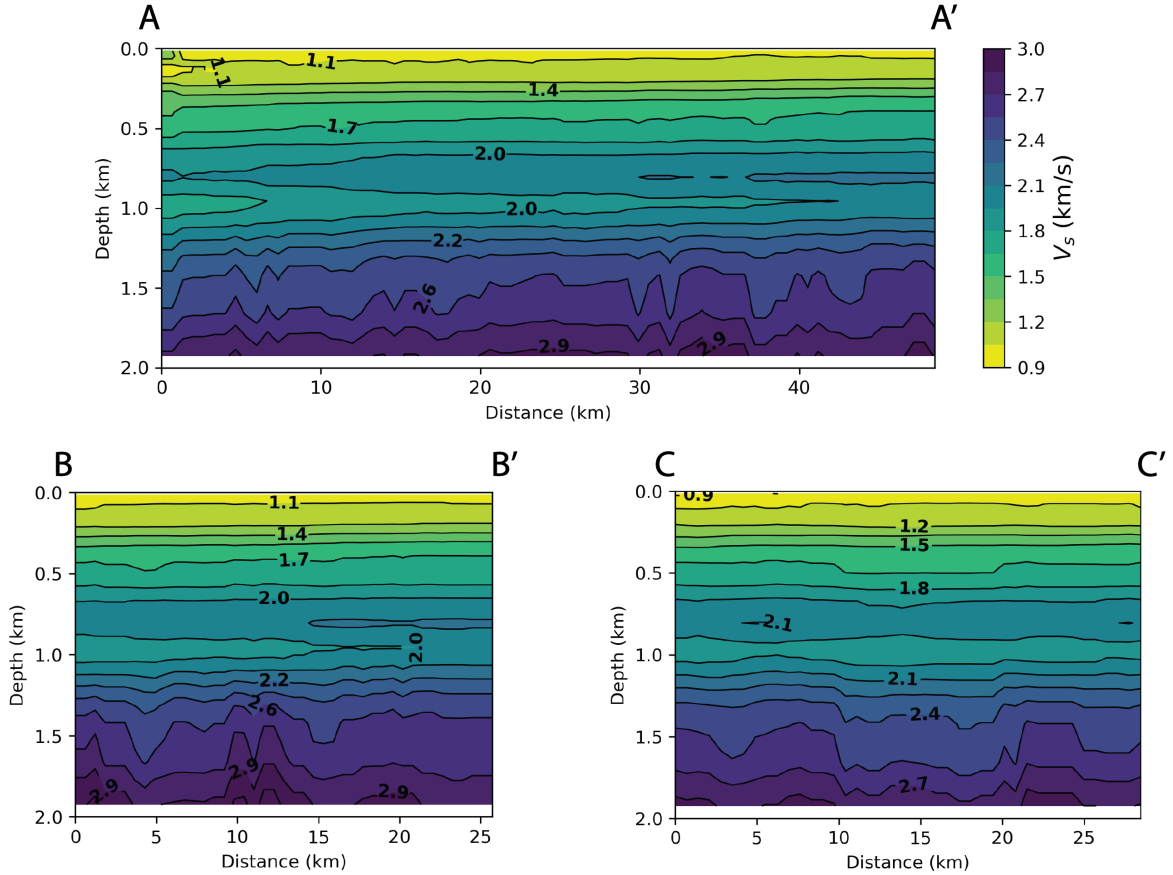


Figure S6. Shear-wave velocity (V_s) cross-sections along A–A’, B–B’, and C–C’ in Figure S5. The V_s values marked on the contours are in units of km/s. The depth of the crystalline basement is around 2.3 km (Crain & Chang, 2018). The V_s decreases rapidly at shallow depth but transits gently in the lateral direction. Note that the vertical scale is 20 times exaggerated. The largest vertical V_s transitions are within the top 0.4 km and between 1 – 1.3 km. We assume the site term for attenuation dominates in the upper 0.4 km to calculate the site-dependent Quality Factor.

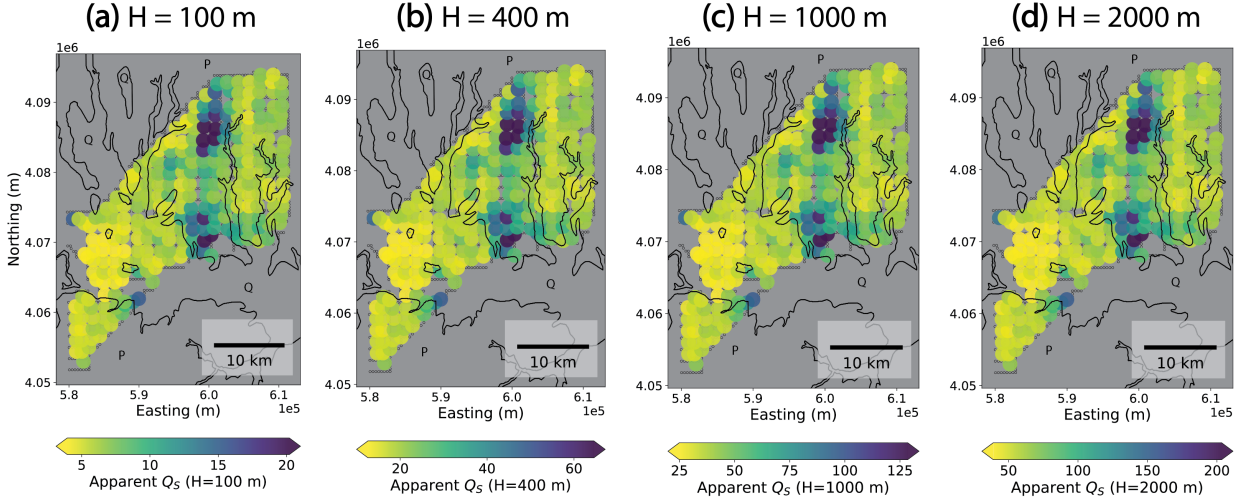


Figure S7. Map of the Quality Factor for S waves (Q_s) derived from $\kappa_{0,s,acc}$ and the shear-wave velocity (V_s) structure. We assume site-dependent attenuation for regional events associated with structures in the top H m. Results from left to right assume $H = \text{(a)} 100$ m, $\text{(b)} 400$ m, $\text{(c)} 1000$ m, and $\text{(d)} 2000$ m, respectively. Each colored circle represents a subarray consisting of stations within a 2.5 km diameter circle (15 – 20 stations; small black hollow circles). Different H assumptions shift the range of Q_s but do not change the pattern significantly because the lateral variation of V_s (and therefore travel time in Equation 7) does not change significantly across these depths. The color ranges exclude the 1% lowest and highest values for visualization. The contours indicate the boundaries of the surficial Quaternary formations (Q) versus the Permian formations (P).

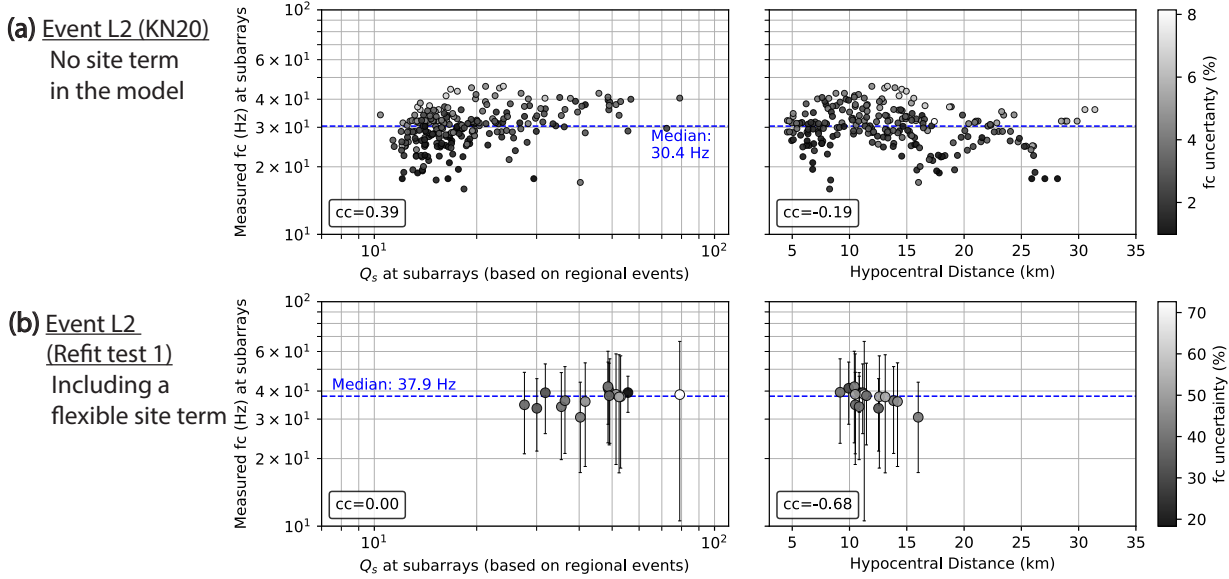


Figure S8. Corner frequency (f_c) measurements of Event L2 in **(a)** Kemna et al. (2020) (KN20), and **(b)** refit test 1. Left: f_c vs the actual Q_{site} (i.e., Q_s). Right: f_c vs the hypocentral distance. The color scales indicate fitting uncertainty (standard deviation of f_c)/ f_c × 100%). The error bars indicate the standard deviation. The horizontal dashed lines are the median f_c . Each point represents a subarray with 15 – 20 stations within a 2.5 km diameter circle.

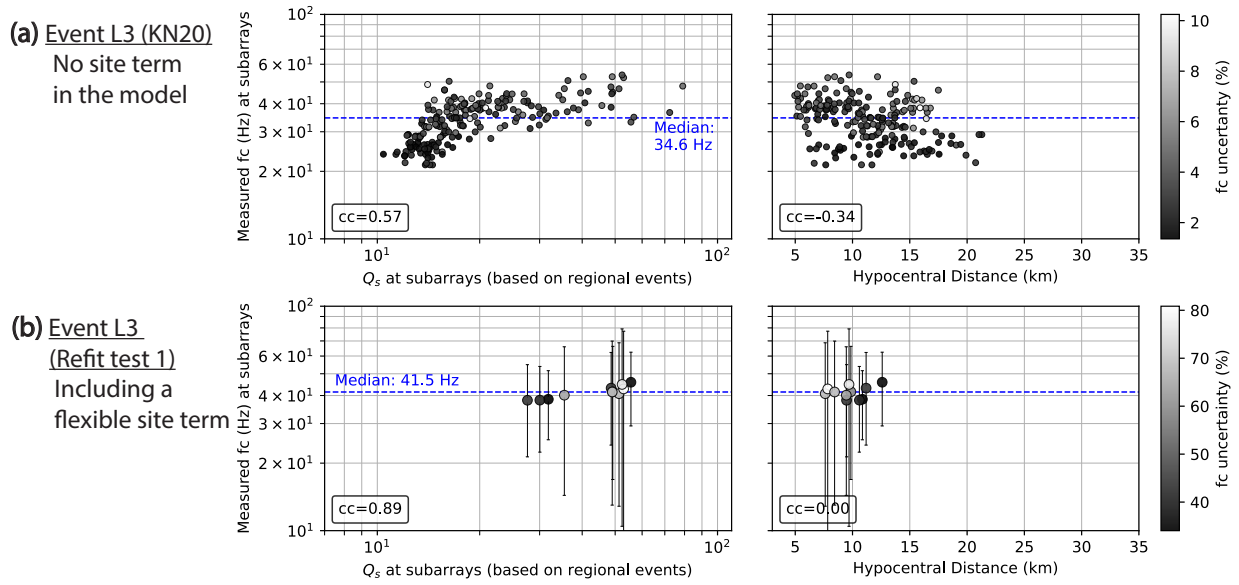


Figure S9. Corner frequency (f_c) measurements of Event L3 in **(a)** Kemna et al. (2020) (KN20), and **(b)** refit test 1. Left: f_c vs the actual Q_{site} (i.e., Q_s). Right: f_c vs the hypocentral distance. The color scales indicate fitting uncertainty (standard deviation of f_c)/ f_c × 100%). The error bars indicate the standard deviation. The horizontal dashed lines are the median f_c . Each point represents a subarray with 15 – 20 stations within a 2.5 km diameter circle.

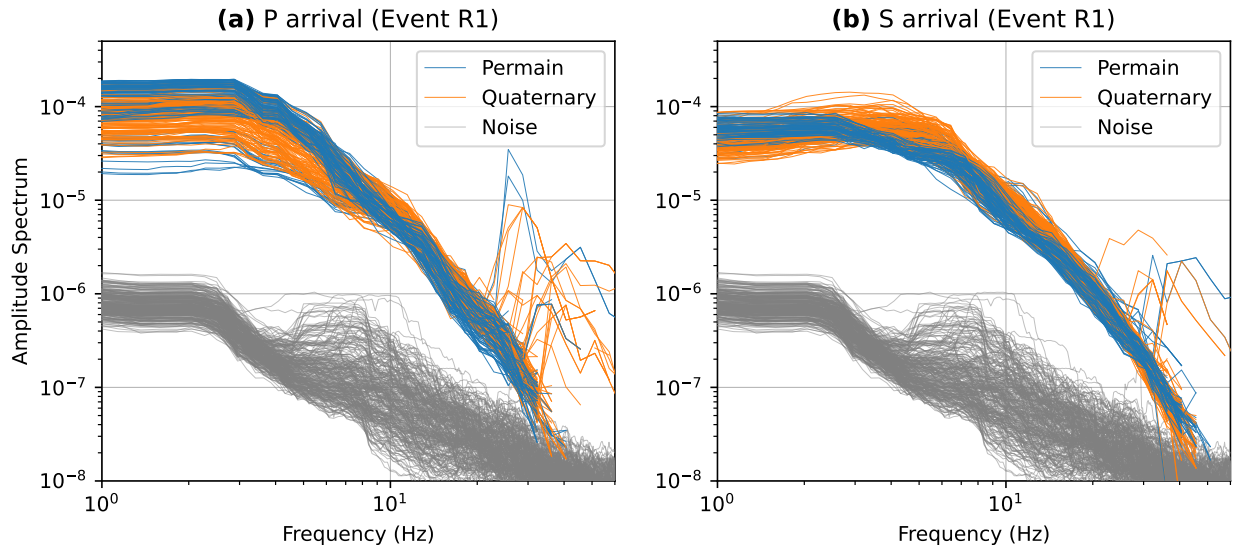


Figure S10. (a) P arrival and (b) S arrival spectra for event R1. The colors indicate the dominant surficial formation. The arrivals are cut between -0.2 and 2.0 s around the arrival times. The noise spectra (gray) are calculated in a window with the same length which is 8 s before the P arrivals. Each spectrum is stacked among stations within subarrays. Each subarray includes stations within a 2.5 km diameter circle (15 – 20 stations). Spectra on the Quaternary sediments (orange) experience higher motion than those on the Permian sandstones (blue) between 8 and 25 Hz. The narrow-banded amplification related to shallow Quaternary formations (Chang et al., 2024) might cause the high apparent Q_{total} and apparent n (Figure 9(b)) in Kemna et al. (2020). Note that the amplitude difference below 8 Hz might contain non-negligible influences from source radiation pattern (Chang et al., 2023). In refit tests 1 – 3, we restrict our analysis to only the Permian sites to avoid the amplification effects not included in our simple model.

Name	Event Time (UTC)	Latitude	Longitude	Depth (km)	Magnitude Type	Magnitude
R1	2016-04-27T15:44:55	35.7422	-97.1777	6.09	M_{wr}	3.7
R2	2016-04-26T15:44:11	35.5201	-97.0899	6.892	M_{wr}	3.6
R3	2016-04-26T18:46:51	35.7276	-97.1616	5.0	M_{wr}	3.6

Table S1. List of the three regional events in Central Oklahoma (U.S. Geological Survey) that we used for measuring the attenuation.

Name	Event Time (UTC)	Latitude	Longitude	Depth (km)	Magnitude Type	Magnitude
L1	2016-05-03T10:35:01	36.8027	-97.7982	6.050	M_L	2.757
L2	2016-04-16T05:09:08	36.8342	-97.8068	4.510	M_L	2.195
L3	2016-04-16T08:53:23	36.8735	-97.9217	4.960	M_L	1.911

Table S2. List of three local earthquakes (within the LASSO array) that were recorded by the largest number of stations (Cochran et al., 2020). We use these three events for analyzing station-wise corner frequency variability in Section and . M_L is the local magnitude.

References

- Beyreuther, M., Barsch, R., Krischer, L., Megies, T., Behr, Y., & Wassermann, J. (2010). ObsPy: A Python toolbox for seismology [Software]. *Seismological Research Letters*, 81(3), 530–533.
- Chang, H., Abercrombie, R. E., Nakata, N., Pennington, C. N., Kemna, K. B., Cochran, E. S., & Harrington, R. M. (2023). Quantifying site effects and their influence on earthquake source parameter estimations using a dense array in Oklahoma. *Journal of Geophysical Research: Solid Earth*, (pp. e2023JB027144).
- Chang, H., H., Q., Zhang, Z., Nakata, N., & Abercrombie, R. (2024). Investigation of site amplifications using ambient-noise-derived shallow velocity structures under a dense array in Oklahoma. Manuscript submitted for publication.
- Cochran, E. S., Wickham-Piotrowski, A., Kemna, K. B., Harrington, R. M., Dougherty, S. L., & Peña Castro, A. F. (2020). Minimal clustering of injection-induced earthquakes observed with a large-n seismic array. *Bulletin of the Seismological Society of America*, 110(5), 2005–2017.
- Crain, K. D. & Chang, J. C. (2018). Elevation map of the top of the crystalline basement in Oklahoma and surrounding states. *Oklahoma Geol. Surv. Open-File Rept. OF1-2018*.
- Johnson, K. S. & Luza, K. V. (2008). *Earth sciences and mineral resources of Oklahoma*. Oklahoma Geological Survey.
- Kemna, K., Peña Castro, A., Harrington, R., & Cochran, E. S. (2020). Using a large-n seismic array to explore the robustness of spectral estimations. *Geophysical Research Letters*, 47(21), e2020GL089342.
- Ktenidou, O., Abrahamson, N., Darragh, R., & Silva, W. (2016). A methodology for the estimation of kappa (κ) from large datasets, example application to rock sites in the NGA-East database, and implications on design motions. *PEER Report 2016*, 1.

- Newville, M., Stensitzki, T., Allen, D. B., Rawlik, M., Ingargiola, A., & Nelson, A. (2016). LMFIT: Non-linear least-square minimization and curve-fitting for Python [Software]. *Astrophysics Source Code Library*, (pp. ascl-1606).
- Nye, T., Sahakian, V. J., King, E., Baltay, A., & Klimasewski, A. (2023). Estimates of κ_0 and effects on ground motions in the San Francisco Bay Area. *Bulletin of the Seismological Society of America*, 113(2), 823–842.
- Rubinstein, J. L., Ellsworth, W. L., & Dougherty, S. L. (2018). The 2013–2016 induced earthquakes in Harper and Sumner Counties, southern Kansas. *Bulletin of the Seismological Society of America*, 108(2), 674–689.
- U.S. Geological Survey (2022). Earthquake Hazards Program Advanced National Seismic System (ANSS) Comprehensive Catalog of Earthquake Events and Products: Catalog ($m > 3$) in Central Oklahoma (2016-04-14–2016-05-10) [data set]. Last accessed on 2022-09-19.